ARTICLE   OPEN

Check for updates

Two quasi-interfacial *p-n* junctions observed by a dual-irradiation system in perovskite solar cells

Mohamed I. Omer[1,2,8], Tao Ye[1,3,8], Xianqiang Li[1,2], Shaoyang Ma[2], Dan Wu[2], Lei Wei[2], Xiaohong Tang[2], Seeram Ramakrishna[4], Qiang Zhu[1], Shanxing Xiong[5], Jianwei Xu[1,6,7 ✉], Chellappan Vijila[1 ✉] and Xizu Wang[1,8 ✉]

In general, perovskite solar cells (PSC) with a sensitized or thin-film architecture absorb light from a single-side illumination, and carrier separation and transport only take place inside the active layer of the perovskite film. Herein, we demonstrated a dual-irradiation PSC system in which light passes through both the fluorinated tin oxide (FTO) side and the Au electrode side, resulting in much faster interfacial charge carrier extraction and transportation than that in a single-irradiation system, in which light passes through from either the FTO or semitransparent Au electrode side. This dual-irradiation PSC system with a configuration of FTO/Cl-TiO_2/Mp-TiO_2/mixed perovskite/spiro-OMeTAD/Au/ITO can form two quasi-interfacial *p-n* junctions, which occur separately at the interfaces of TiO_2/perovskite and perovskite/spiro-OMeTAD. When the PSC device was illuminated simultaneously from both the FTO and Au/ITO sides, the PSC achieved a total power conversion efficiency (PCE) as high as 20.1% under high light intensity (1.4 sun), which is higher than PCE (18.4%) of a single-irradiation system. The time of flight (TOF) photoconductivity, small perturbation transient photovoltaic (TPV), finite-difference time-domain (FDTD) optical simulations, and dual illumination-side-dependent impedance spectroscopy (ISD-IS) were used to authenticate the presence of two quasi-interfacial *p-n* junctions in the PSC, creating more charge carriers than only one quasi *p-n* junction, and thus leading to a fast recombination process.

INTRODUCTION

Lead halide perovskite $APbX_3$ [A = Cs (cesium), MA ($CH_3NH_3^+$, methylammonium), and FA (NH = $CHNH_3$, formamidinium); X = Cl, Br, and I] solar cells are strong competitors of the traditional silicon solar cells and III–V solar cells due to its unique optoelectronic properties, such as optical tunability, high absorption coefficients, millimeter-scale charge carriers diffusion length as well as easy fabrication[1–11]. The latest highest certificated power conversion efficiency (PCE) of the perovskite solar cell (PSC) is over 23% and the reported highest is 25%[12–14] in literature, and the PCE is achieved with a mixed perovskite light absorber fabricated through a two-step intramolecular exchanging process[1,8]. In contrast, the PSC fabricated with a one-step deposition of mixed perovskite light absorber [$FA_{0.81}MA_{0.15}Pb(I_{0.836}Br_{0.15})_3$] can achieve an almost comparable PCE (21.6%)[9–11,15,16] to the highest certificated one. Tremendous attention has been paid to the mixed perovskites that are fabricated through mixing cations and halides. This is because pure $APbI_3$-based perovskites show numerous disadvantages in the solar cell fabrication, for example, unfavorable structural phase transition and light-induced trap-state ($MAPbI_3$), degradation upon contact with moisture and solvents ($MAPbI_3$ and $FAPbI_3$), the formation of photo-inactive hexagonal δ-phase and photoactive α-phase during crystallization ($FAPbI_3$), and the formation of photo-active phase ($CsPbI_3$) at high temperature[8,17–25]. Mixed perovskite systems have shown the integrated advantages of the constituents while avoiding the aforementioned weaknesses[8–11,26].

Some transparent electrodes that allow light to go into the device from both electrode sides have been developed in some early photo-electrochemical devices[27–29]. However, in all the existing PSCs even including other type photovoltaic devices[30–34], light always goes into the device from the transparent conductive electrode side and the incident light only comes from a single light source. The rear metal electrode mainly functions as a reflector to generate additional energy from the diffused light and the reflected light to enhance to some extent the absorption efficiency. Unlike a traditional PSC with a thick real metal electrode, the thickness of the rear metal electrode in this work is reduced from 60–120 nm to 15–30 nm, and transparent indium tin oxide (ITO)[35–37] is deposited onto a thin Au layer to form a semitransparent Au/ITO electrode[38], allowing more light to pass through the rear layer. Our work showed that this dual-irradiation PSC system allowing light to enter the system from both sides gave a PCE of 20.1 ± 0.8% under a dual-irradiation condition [simulated 1 sun (AM 1.5 G) at the FTO side and a white LED at the Au/ITO side]. We assume that two quasi-interfacial *p-n* junctions that are located at the FTO and Au/ITO sides, respectively, instead of a single *p-n* junction at the FTO side, account for a significant increase in PCE. To examine the photophysics of such a dual-irradiation PSC system, the time of flight (TOF) photoconductivity, small perturbation transient photovoltaic (TPV), finite-difference time-domain (FDTD) optical simulations were performed, collectively revealing that fast interfacial charge extraction and transportation occurring at the two quasi *p-n* interfaces are

[1]Institute of Materials Research and Engineering (IMRE), Agency for Science, Technology and Research (A*STAR), #08-03, 2 Fusionopolis Way, Innovis, Singapore 138634, Singapore. [2]School of Electrical and Electronic Engineering, Nanyang Technological University, 50 Nanyang Avenue, Singapore 639798, Singapore. [3]Key laboratory of Micro/Nano Systems of Aerospace, Ministry of Education, Northwestern Polytechnical University, Xi'an 710072, China. [4]Department of Mechanical Engineering, National University of Singapore, Singapore 117576, Singapore. [5]College of Chemistry and Chemical Engineering, Xi'an University of Science and Technology, Xi'an 710054, PR China. [6]Department of Chemistry, National University of Singapore, 3 Science Drive 3, Singapore 117543, Singapore. [7]Institute of Sustainability for Chemicals, Energy and Environment (ISCE2), 1 Pesek Road, Jurong Island, Singapore 627833, Singapore. [8]These authors contributed equally: Mohamed I. Omer, Tao Ye, Xizu Wang. ✉email: Xu_Jianwei@isce2.a-star.edu.sg; c-vijila@imre.a-star.edu.sg; wangxz@imre.a-star.edu.sg
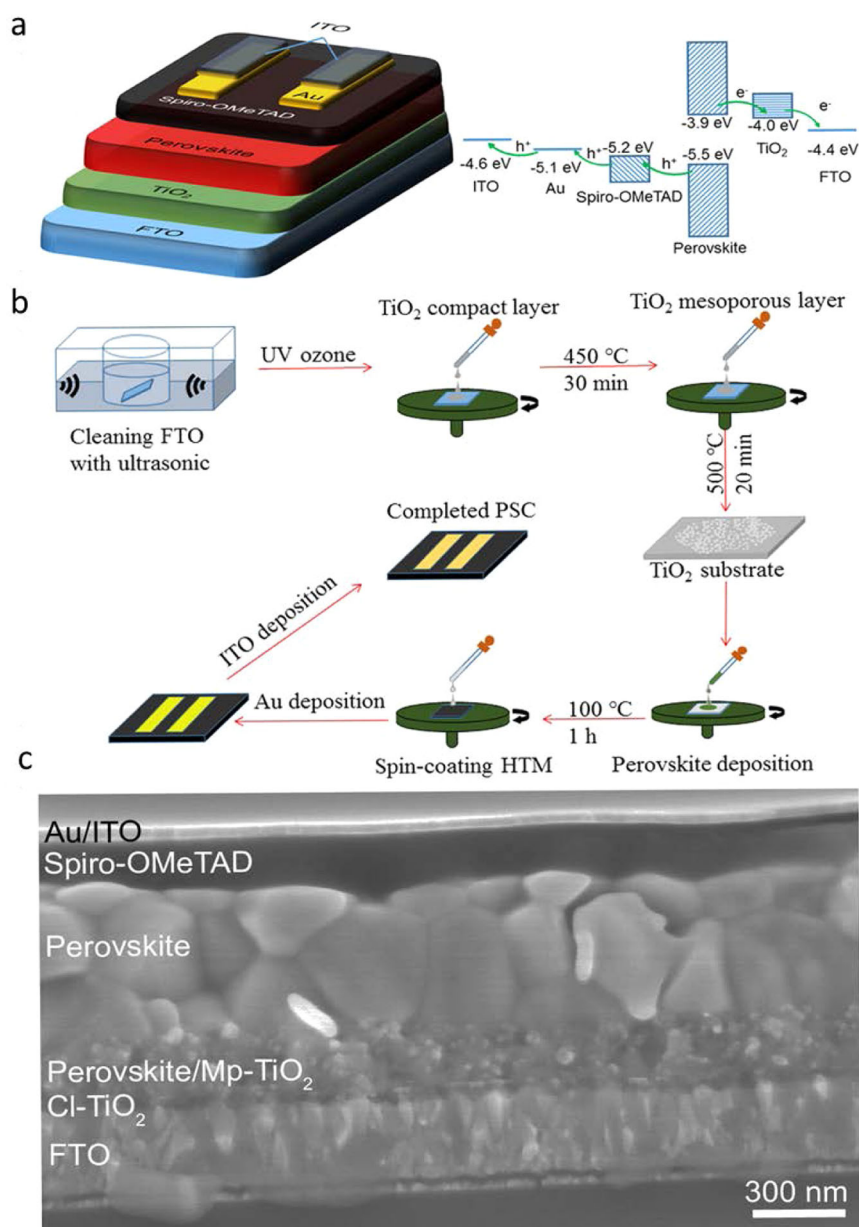
Fig. 1 Fundamentals of the dual-irradiation system. a Left: schematic drawing of the dual-irradiation system, showing a device configuration of FTO/TiO₂/perovskite/spiro-OMeTAD/Au/ITO; Right: the energy level diagram of the device. **b** The fabrication processes of the dual-side function solar cell. **c** The cross-section SEM image of the fabricated device with a 22.5 nm Au layer. Cl-TiO₂ compact TiO₂, Mp-TiO₂ mesoporous TiO₂, spiro-OMeTAD 2,2′,7,7′-tetrakis[N,N-di(4-methoxyphenyl)amino]-9,9′-spirobifluorene.

responsible for this PCE enhancement. Furthermore, the illumination-side-dependent impedance spectroscopy (ISD-IS)[39] was used to infer the dominant recombination pathway (e.g., interface or bulk) and validate the presence of two quasi-interfacial *p-n* junctions in the PSC. Our PSC structure with a dual-irradiation configuration offers a new insight into perovskite photovoltaic physics and device integration, and this type of novel PSC dual-irradiation systems is potentially useful for many applications.

RESULTS

Preparation of the semitransparent Au/ITO electrode
The dual-irradiation device structure with a configuration of FTO/Cl-TiO₂/Mp-TiO₂/mixed perovskite/spiro-OMeTAD/Au/ITO, and the energy levels[15,26,40] of different device components is

shown in Fig. 1a, b. The cross-section scanning electron microscope (SEM) image of the PSC device is shown in Fig. 1c, which illustrates the thickness and morphology of each functional layer of the device. An enlarged cross-sectional SEM image of the Au/ITO electrode is given in Supplementary Fig. 1, displaying that the ITO is well deposited onto the top of the thin-film Au.

When light enters the device, the perovskite layer absorbs light and generates free holes and electrons. The free electrons transport through the TiO₂ layers to the FTO electrode, while the free holes are extracted through the spiro-OMeTAD layer and collected by the Au/ITO electrode. The details of device fabrication are given in the Methods section. The fabricated ITO layer properties were investigated through SEM, atomic force microscope (AFM), X-ray photoelectron spectroscopy (XPS) and ultraviolet photoelectron spectroscopy (UPS) methods. An SEM image shown in Supplementary Fig. 2a shows that the ITO surface is
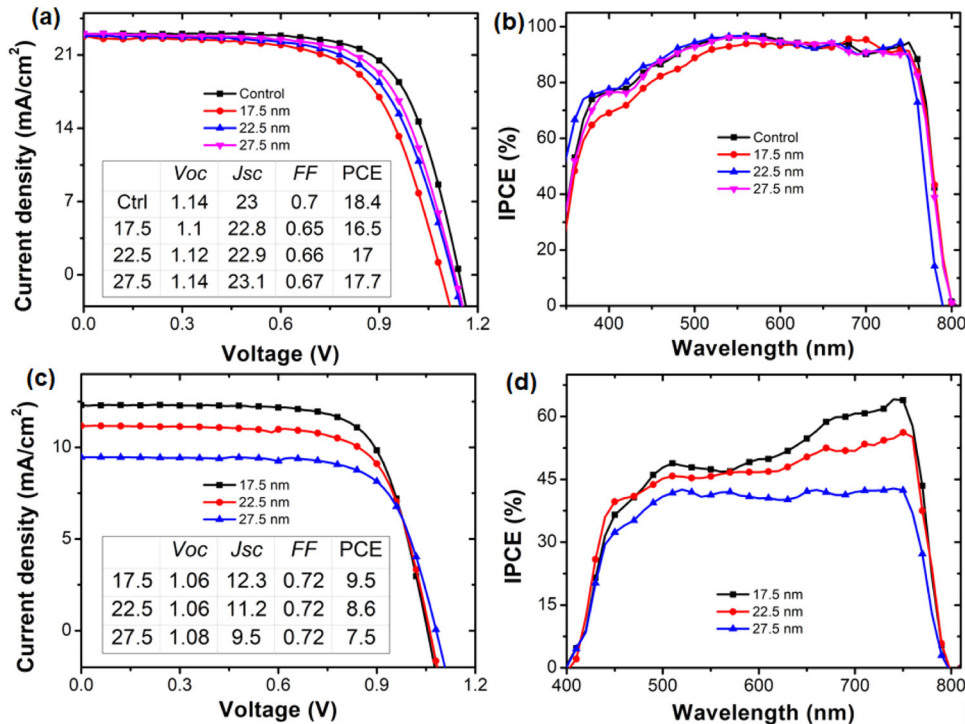
Fig. 2 Single-irradiation photovoltaic parameters. a, b J–V curve and IPCE of different devices obtained from irradiation at the FTO sides, **c, d** J–V curve and IPCE of different devices obtained from irradiation at the ITO sides. Control: device with an 80 nm Au single electrode.

compact and smooth, and the surface morphology of our prepared ITO layer is identical with the commercial ITO sample. The average roughness (R_a) of the ITO layer for this sample estimated by AFM (Supplementary Fig. 2b) is 2.5 nm. XPS experiment was conducted to study atomic and electronic structures of the prepared ITO layer. XPS elemental spectra of In_{3d}, Sn_{3d}, and O_{1s} of the sample are shown in Supplementary Fig. 2c–e. The binding energy of In_{3d}, Sn_{3d}, and O_{1s} obtained from the XPS spectra shows that the ITO precursor is successfully transformed into the ITO, which is consistent with the literature[27,41–43]. UPS was used to determine the work function of the prepared ITO layer, and the measured work function of our ITO layer was ~4.6 eV, (Supplementary Fig. 2f) which is similar to those of some recently reported ITO materials for various transparent conductive electrodes[41–43]. Compared to commercial ITO glass (Supplementary Fig. 3), our prepared ITO achieved the same surface flatness.

Single-side Illumination

Current density–voltage (J–V) curves and corresponding incident photon-to-electron conversion efficiency (IPCE) spectra obtained from the FTO and ITO side illumination are shown in Fig. 2. According to the J–V results, it was observed that the performance of the devices with semi-transparent ITO electrodes was dependent on the thickness of the Au electrodes. For the device with the thinnest Au electrode (17.5 nm), its PCE when irradiation is at the FTO side is slightly lower due to the insufficient free holes collection at the thin Au layer. However, the thin Au layer can let more light in from the ITO side, and therefore a higher PCE is achieved when light irradiation is at the ITO side. When the thickness of the Au electrode is increased, nearly all the photovoltaic (PV) parameters including open circuit voltage (V_{oc}), short current density (J_{sc}), fill factor (FF), and PCE obtained from illumination at the FTO side are enhanced (Fig. 2a). In contrast, all PV parameters in particular for J_{sc} are going down for illumination at the ITO side (Fig. 2c). The IPCE profiles and values

obtained from illumination at the FTO side are similar and only slightly increase with the increase of the thickness of the Au electrode from 17.5 nm to 27.5 nm (Fig. 2b). However, the IPCE is enhanced at a wide wavelength range of 400–800 nm (especially between 600 and 800 nm due to the light attenuation of the Au electrode, (Fig. 2d) when the Au electrode decreases from 27.5 nm to 17.5 nm. Therefore, in order effectively to compare the effect of the direction of the illumination side on the PV performance, we chose 22.5 nm gold electrodes for all the device fabrication.

To study the relationship between the light intensity and J_{sc}, V_{oc}, and FF, a PSC device with a 22.5 nm-Au electrode was illuminated from the FTO and ITO sides, and the curves of J_{sc}, V_{oc}, and FF vs the light intensity are plotted and shown in Supplementary Figs. 4 and 5, respectively. The log (J_{sc}) values almost linearly increase with the log (light density) when illumination at the FTO side or the ITO side. The V_{oc} of the device is not remarkably changed when illumination at the FTO side, but the FF and J_{sc} of the device show significant changes. In particular, the FF decreases due to the increased free carrier recombination derived from the rapid increase of the free carrier density when the light intensity increases. However, the increased free carrier density also leads to the J_{sc} improvement of the device. As for the ITO side, we observed the same trend of the PV parameters for the same device (Supplementary Fig. 5). However, owing to the light attenuation of the Au electrode, the carrier density of the ITO side is lower than that in the FTO side, and the decrease in FF is not significant when the J–V curves are measured from the ITO side with below 1 sun. Thus, the J_{sc} values from both the FTO and ITO sides show a linear relationship (Supplementary Figs. 4 and 5) with the simulated light intensity, indicating the charge carriers recombination caused by defects is low in the device[39–43].

Dual-side illumination

A white LED was utilized to provide another light source for the performance measurement of the same device, and the full light spectrum of the LED can be found in Supplementary Fig. 6[44].
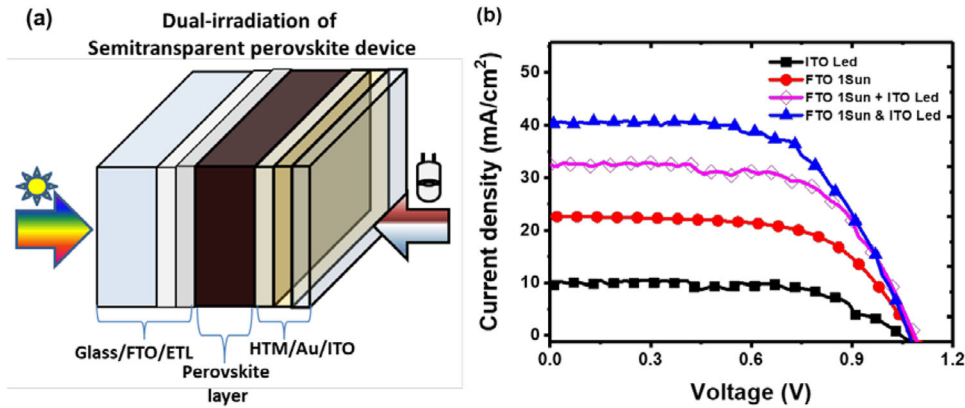
Fig. 3 Dual-irradiation photovoltaic parameters of semitransparent devices. a Schematic drawing of a dual-irradiation testing setup; **b** J–V curve of devices with the Au-22.5 nm/ITO under single or dual irradiation with one or two light sources, respectively. (LED light goes in from the ITO side and 1 sun simulated light goes in from the FTO side). ETL electron-transport layer, HTM hole-transport material.

Table 1. Photovoltaic parameters for the Au-22.5 device measured under different light intensity conditions.

Irradiation conditions[a]	V_{oc} (V)	J_{sc} (mA/cm^2)	FF	PCE (%)
ITO LED (400 W/m^2)	1.06	11.2	0.72	16.6 ± 0.8
FTO solar simulator (1000 W/m^2)	1.12	22.9	0.67	17.0 ± 0.5
ITO LED + FTO solar simulator (1000 + 400 W/m^2)[b]	1.08	32.4	0.65	16.2 ± 0.6
FTO solar simulator (1400 W/m^2)	1.09	31.1	0.45	10.9 ± 0.3
Dual-irradiation (ITO LED & FTO solar) (1400 W/m^2)	1.08	40.4	0.64	20.1 ± 0.8

[a]All the PV parameters are calculated at specific light intensity.
[b]The sum of J–V curves of ITO LED + FTO solar simulator under the sum of two irradiation light intensity, 1400 W/m^2.

Figure 3a schematically shows the testing system of the device under dual-irradiation conditions. The J–V curves of the PSC device based on different irradiation conditions are given in Fig. 3b, and the corresponding data are summarized in Table 1. More specifically, an overall PCE of 16.6% with a V_{oc} of 1.06 V, a J_{sc} of 11.2 mA/cm^2, and an FF of 0.72 was achieved under the LED illumination at the ITO side. In contrast, an overall PCE of 16.5% with a V_{oc} of 1.10 V, a J_{sc} of 22.6 mA/cm^2, and an FF of 0.67 was obtained under the simulated 1 sun illumination at the FTO side. Based on the performance characteristics of unilaterally irradiated PSCs[45], the estimated PCE after illumination at both sides should be around 16.2% as the light intensity increases at 1.4 sun. It is surprising that when the device works under the dual irradiation condition at same time (LED light goes in from the ITO side and 1 sun light goes in from the FTO side), an enhanced PCE over 20.1% has been observed with a V_{oc} of 1.08 V, a J_{sc} of 40.4 mA/cm^2, and an FF of 0.64. Thus, the overall device performance enhancement can be achieved for the device when the white LED is utilized as the second light source and illuminates at the ITO side of the device[46]. The PCE is higher than that of single-side irradiation under high light intensity (1.4 sun) and greater than the combined value when irradiation at the ITO and FTO sides, as shown in Fig. 3b. This inspiring improvement in PCE under the dual-irradiation system impels us to investigate its optical/electronic conversion mechanism.

Optical simulations

The increase in J_{sc} from 32.4 to 40.4 mA/cm^2 under the dual-irradiation system may be due to the high optical absorption efficiency in the dual-irradiation system. Therefore, to investigate the absorption property of the perovskite layer under illumination at the FTO and ITO sides, we built an optical model using the optical admittance analysis technique[47,48] and the FDTD simulations[11,49,50] to estimate the optical energy distribution within the perovskite layer. However, according to the simulation results, the energy flux of the perovskite layer under the dual-irradiation conditions was comparable to the sum of those under the single irradiation at the ITO and FTO sides, separately. As a result, the dual-irradiation is in fact not able to increase the total amount of incident photons in the perovskite layer, implying that the increase in photocurrent does not stem from the light distribution instead of from another route.

As show in Fig. 4, the FDTD simulation of the spatial distribution of E-field at 450, 550 and 600 nm within the Au-22.5 device in the single and dual-irradiation systems. Three scenarios were simulated: illumination at both the ITO and FTO sides, the FTO side and the FTO side, respectively. When illuminated from the FTO or ITO side only, no, or very weak standing waves can be formed within the perovskite layer. In contrast, the strong standing waves can be formed at a certain wavelength when the perovskite solar cell is illuminated from both sides. The magnitude of standing waves at 600 nm is much stronger than that at both 450 and 550 nm. Since the main peak of the LED spectra is located at around 600 nm, in good agreement with the optical admittance analysis and optical transmittance results (Supplementary Figs. 4 and 7). It is worth noting the most energy flux of incident light always locates at the two interfacial regions (Fig. 4) in the device. Meanwhile, the optical admittance analysis (Supplementary Fig. 8) also shows that nearly 80% of the incident light energy is absorbed within the first ~100 nm of the perovskite layer interface regardless of the light propagating direction. We believe that the strong standing waves generated in the proximity of two interfaces within the perovskite layer have a positive effect on improving the device performance.

Charge carrier transport mechanisms

Based on above simulation, we propose that the increased photocurrent mainly originates from the more efficient interfacial charge carrier collection in the dual-irradiation perovskite device. Figure 5a shows the schematic diagram of the charge carriers generation and separation within the device under the dual irradiation system. The perovskite ambipolar properties and the capability to transport both photo-generated free holes and electrons, have been observed in recent studies[51,52]. Here, we demonstrated that two quasi p-n junctions, which locate at the TiO$_2$/perovskite and perovskite/spiro-OMeTAD interfaces, can co-exist for fast interfacial charge carrier collection in the dual-irradiation system. Therefore, the charge carrier extraction and
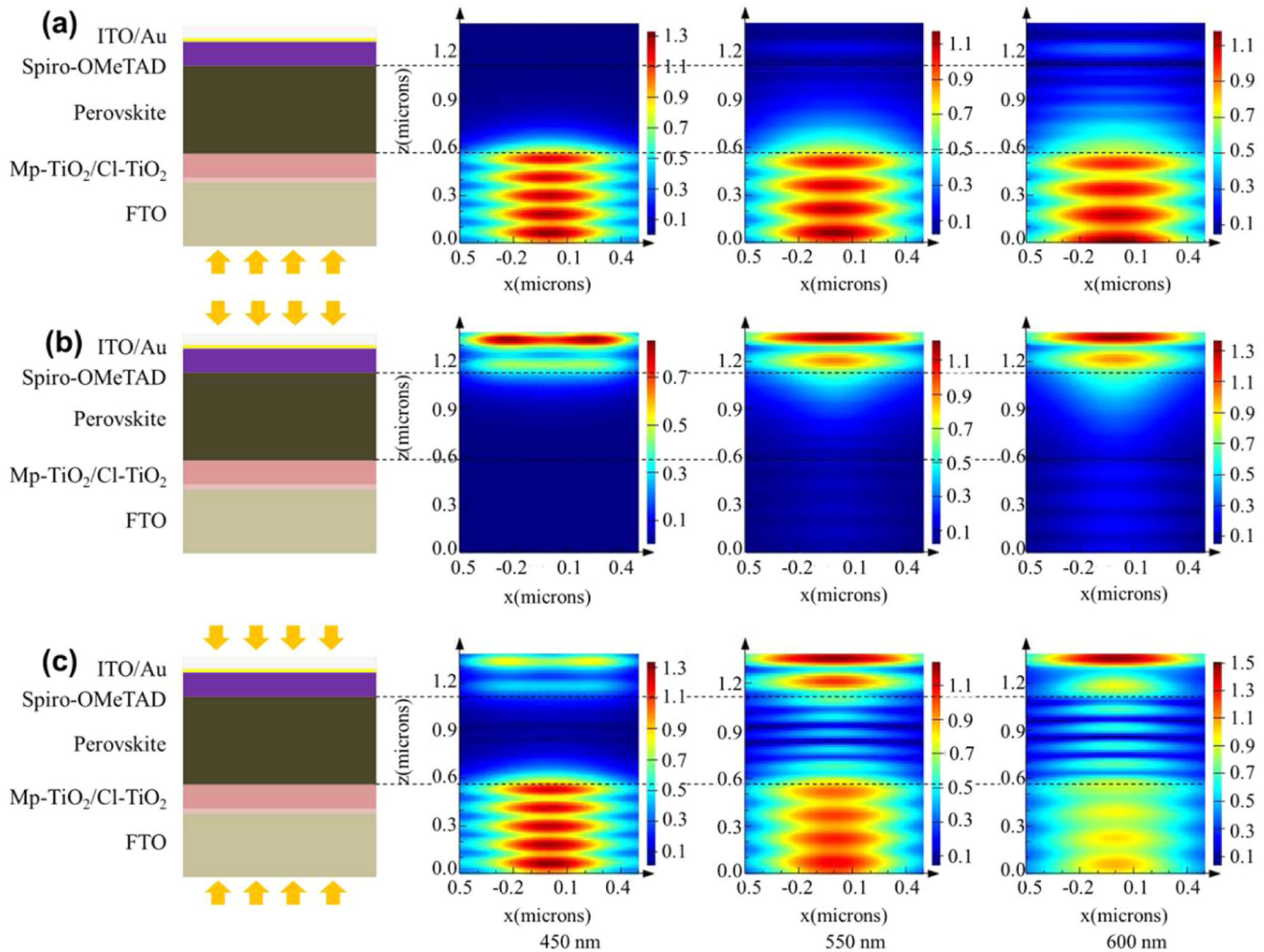
Fig. 4 Spatial distribution of the E-field at 450 nm, 550 nm, and 600 nm within the Au-22.5 device. a illumination at the FTO side; **b** illumination at the Au/ITO side; **c** illumination from both ITO and FTO sides.

transport are expected to be more efficient in the dual-irradiation device than that in the single-irradiation bulk device. To throw further light on this conjecture, we conducted TOF photoconductivity and small perturbation TPV[7,11,52–57] measurements, and results are shown in Fig. 5b, c, respectively.

Charge carriers mobilities in this device are also studied with the TOF technique at room temperature[7,11,52]. By simply changing the applied voltages of the device, the electron and hole transit time can be obtained separately. Furthermore, the charge carriers mobilities within the system can be easily calculated using the heterojunction thickness, the applied back voltage and the free charge transit time. Supplementary Fig. 9 shows the log-log plots of the TOF transits spectra for free holes and electrons at the FTO and ITO sides, respectively. Transit times can be obtained from the log-log plots of the TOF spectra, and the charge mobility (μ) in the system can be further calculated with the relation $\mu = d^2/Vt_T$, where d is the hole or electron transporting lengths before reaching the electrodes (Au for holes and FTO for electrons), V is the applied voltage, and t_T is the transit time. The charge carrier mobility is essentially the same regardless the irradiation side of the laser beam. From the TOF results in Fig. 5b, the magnitude of hole and electron mobility at the FTO and Au/ITO side irradiation is almost similar, indicating balanced charge carrier mobility at both interfaces of the device. In the small perturbation TPV measurement with open circuit voltage conditions, voltage transients are generated by background white light illumination,

and small perturbation was created using a nanosecond laser pulse of wavelength 532 nm. The charge carrier relaxation times (τ) at different irradiation conditions are shown in Fig. 5c (its full spectra can be found in Supplementary Fig. 10). The τ value (304 µs) obtained from the ITO side irradiation is longer than that obtained from the FTO side (258 µs), and they are approximately in the same order of magnitude. In contrast, the dual-irradiation system exhibits a significantly shorter τ value (50 µs) in comparison with these τ values that are obtained from single-irradiation systems. In a dual-irradiation system, two quasi p-n junctions occurring at the two interfaces and the diffusion of excess electrons and holes towards the bulk may trigger a higher order charge recombination process, and thus a shorter carrier lifetime than that obtained in the single-side irradiation was observed. Compared with the single-irradiation model, the PSC devices have a higher rate of charge recombination and a shorter carrier lifetime in the dual-irradiation system at the same incident light intensity. This also implies that our two quasi p-n junction model in PSC device enables to create more charge carriers than one quasi p-n junction model only, leading to a fast recombination process.

Impedance spectroscopy is a powerful tool to study electrochemical systems and solid-state devices, and recently it has also found applications for photovoltaic materials and devices such as dye sensitized solar cells (DSSC)[58], organic photovoltaics (OPV)[59], and perovskite photovoltaics[60], to in situ monitor transport and
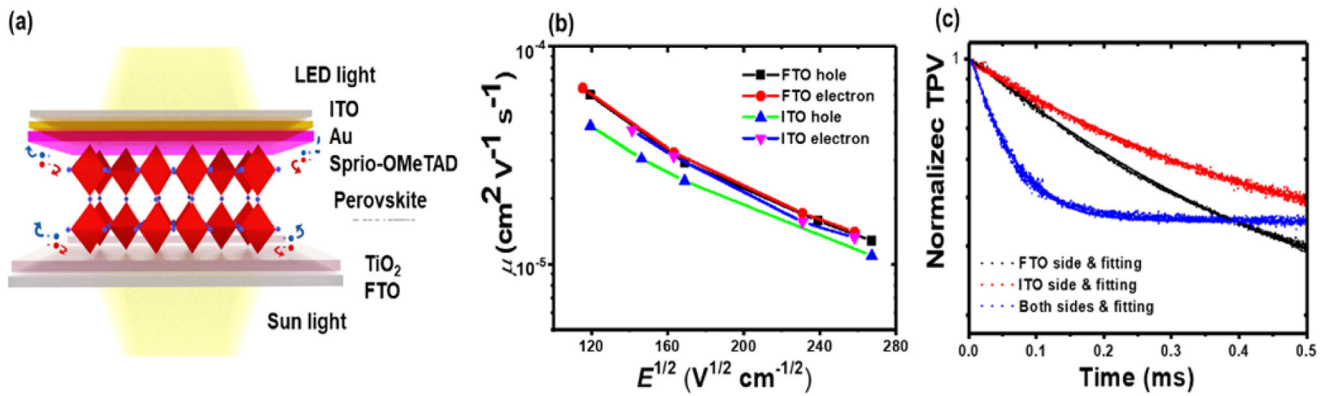
Fig. 5 **Charge carrier transport within the device.** a Schematic illustration of the mechanism of the charge carriers generation and separation within the semitransparent perovskite device under dual irradiation. b TOF spectra of a semitransparent perovskite device from both FTO and ITO irradiation. c A log plot of TPV of the perovskite device under three different irradiation conditions.
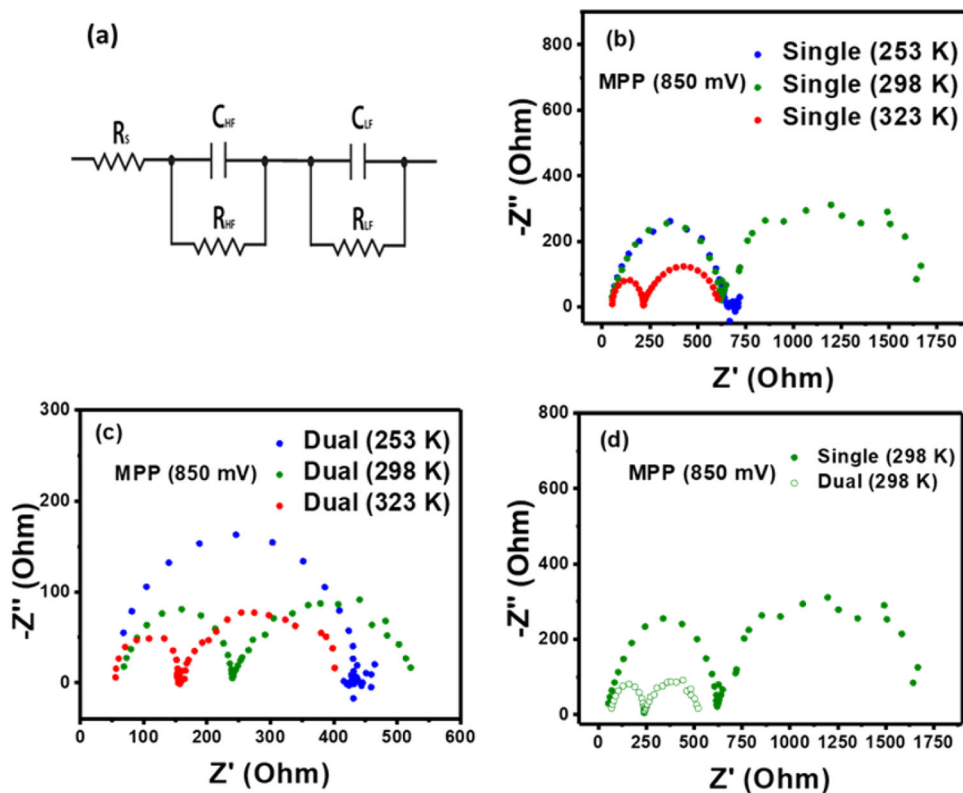

Fig. 6 **The Nyquist plots of ISD-IS patterns.** Schematized strategies quasi *p-n* junction simple RC Voigt circuit element, for perovskite solar cell (**a**), Nyquist plots of impedance spectra obtained under 1 sun single (**b**), 1 sun and white LED illumination in the vicinity of maximum power at different temperature (**c**), comparison of the Nyquist plots with the single and dual illumination at room temperature (**d**).

recombination processes at different points along the solar cell current−voltage (IV) curve[61–64]. The Nyquist plots of ISD-IS patterns are shown in Fig. 6. For all the spectra, two clear arcs are observed at high frequencies as well as at low frequencies except at low temperature. Unlike bulk heterojunction organic solar cells with a sandwich structure[64,65], these two semicircles are observed frequently in PSCs[62,64], indicative of the existence of two different charge-splitting regions inside the cell, as shown in Fig. 6a. Furthermore, Fig. 6b shows the Nyquist plots measured for the PSCs under single irradiation conditions from the FTO side at three temperature conditions. A single semicircle at low temperature certifies that only one *p-n* junction appears with unilateral illumination and overlaps with the first interface at low-temperature (253 K). However, when the temperature was raised

to room temperature (297 K), the appearance of another semicircle in the high-resistance region indicates the appearance of another splitting interface in the device, and this second interface does not start to show significant exciton splitting until it is greater than that at room temperature (297 K). In contrast, for device with the dual-light irradiation system, it is clearly seen that the semicircle at low temperature is much larger than the two semicircles at room temperature, suggesting that the dual-light irradiation enhances both *p-n* splitting interfaces. However, the first *p-n* splitting interface is still dominant, accompanying with gradual enhancement of the second *p-n* junction splitting as the temperature rises to 323 K In order to visually compare the exciton splitting by single and double illumination (Fig. 6d), it implies that dual illumination can greatly enhance these two *p-n* junctions

splitting efficiency and reduce the migration of positive and negative charges, hence balancing the hole and electron pairs in the device. Thus, the actual photoelectric conversion efficiency is improved by dual-light illumination. These results unequivocally validate that there is a two quasi *p–n* junction's model in our PSC device, and it enables to create more charge carriers than one quasi *p–n* junction only, leading to a fast recombination process. More detail characteristic of ISD-IS are shown in Supplementary Fig. 11 and fitting parameters are listed in Supplementary Table 1.

DISCUSSION

In this work, we have successfully fabricated highly efficient PSCs with a configuration of FTO/Cl-TiO$_2$/Mp-TiO$_2$/mixed perovskite/hole transport material/Au/ITO under a dual-irradiation system. It was observed that the dual-irradiation PSC system exhibited a higher PCE value (20.1%) than the single-irradiation PSC system (17.7%). The optical admittance analysis and the FDTD simulation showed that a majority of the incident light is absorbed in the proximity to the perovskite/TiO$_2$ and perovskite/spiro-OMeTAD interfaces. The TOF and TPV studies also revealed that there is a higher carrier concentration in a dual-irradiation system than in a single irradiation system, resulting in the high order recombination process in the perovskite layer. The performance enhancement of the device under a dual-irradiation system is attributed to the formation of two quasi *p–n* junctions, leading to fast interfacial charge extraction and transportation. The device that absorbs light from both sides would open a new way for enhancing PCE to a higher level than its traditional counterparts. Furthermore, dual ISD-IS was used to prove the presence of two *p–n* junctions at the PSCs device when illumination at both sides. In addition, this type of dual-irradiation PSC systems could be developed to be fully transparent by modulating the optical and electrical characteristics of the rear electrode, and in turn, their applicability can be extended in many other areas such as a substitute for glass walls in buildings particularly those with glass facades, dual-illumination photodetectors, and various sensors. In the future, one of research work may be focused on using high-performance organic hole transporting materials[31–33] to further enhance the PCE of the dual-irradiation/PSC system, hence revealing more unique physics of this kind of dual-irradiation PSCs in comparison with the traditional single-irradiation counterparts.

METHODS

Device fabrication

The FTO glass was cleaned with detergent, deionized water, acetone (Sigma-Aldrich), and isopropanol (Sigma-Aldrich) and treated with UV ozone at 100 °C for 10 min. A ~ 30 nm TiO$_2$ layer was deposited onto top of the FTO glass by spin-coating TiO$_2$ precursor solution at 6000 rpm for 30 s. Then, it was heated at 450 °C for 30 min in air. To prepare the TiO$_2$ precursor solution, titanium isopropoxide (1 mL, Sigma-Aldrich) and 12 M HCl solution (10 μL, Sigma-Aldrich) were diluted with ethanol (10 mL). Then *a* ~ 180 nm mesoporous TiO$_2$ layer was deposited by spin-coating a 30-nm TiO$_2$ nanoparticle paste (Dyesol) in ethanol (1:5.5 in weight ratio) at a speed of 6000 rpm for 30 s. The substrate was then annealing at 500 °C for 20 min. The TiO$_2$ layers were treated with a diluted TiCl$_4$ (50 mM in water, Sigma-Aldrich) solution[7]. Next, perovskite film was deposited on the substrate by a spin-coating process with 2000 rpm for 10 s, followed by 6000 rpm for 45 s in a glovebox, and chlorobenzene (110 μL, Sigma-Aldrich) was then dropped in 8–10 s during the second spin-coating process. The substrate was then heated at 100 °C, 60 min. The precursor solution was prepared by dissolving 0.265 g PbI$_2$ (TCI), 0.037 g PbBr$_2$ (Sigma-Aldrich), 0.011 g MABr, and 0.094 g FAI (Dyesol) in 0.4 mL anhydrous *N,N*-dimethylformamide (Sigma-Aldrich) and

0.1 mL anhydrous dimethylsulfoxide (Sigma-Aldrich). Spiro-OMeTAD (Merck) was further deposited by spin-coating at 3000 rpm for 30 s. The spiro-OMeTAD solution was prepared by dissolving 74 mg spiro-OMeTAD, 28.5 μL 4-tert-butylpyridine (Sigma-Aldrich), 17.5 μL of a stock solution of 520 mg/mL lithium bis (trifluoromethylsulphonyl) imide (Sigma-Aldrich) in acetonitrile (Sigma-Aldrich), and 29 μL of a stock solution of 100 mg/mL tris(2-(1H-pyrazol-1-yl)-4-tert-butylpyridine)-cobalt(III) tris(bis(trifluoromethylsulfonyl) imide) (Sigma-Aldrich) in acetonitrile in 1 mL anhydrous chlorobenzene. Finally, 80 nm of gold was deposited as an electrode by thermal evaporation. As for the devices with the semitransparent Au/ITO electrode, thin gold electrodes (17.5 nm, 22.5 nm, and 27.5 nm) were first deposited on top of the substrates, and then ITO transparent conductor was deposited to complete the devices fabrication. An oxidized target (6 inch in diameter) with In$_2$O$_3$ (Sigma-Aldrich) and SnO$_2$ (Sigma-Aldrich) in a weight ratio of 9:1 was employed for the deposition of the ITO electrode. The ITO electrode was prepared by the DC magnetron sputtering with a power of 10 W, and the deposition rate was estimated to be about 2 nm/min. The base pressure in the sputtering system was ~2.0 × 10^{-4} Pa. During the film deposition, an argon–hydrogen gas mixture was employed. The argon partial pressure was set at ~2.9 × 10^{-1} Pa, and the hydrogen partial pressure varied from 1.1 × 10^{-3} to 4.0 × 10^{-3} Pa to optimize the properties of ITO films.

Optical simulations

The simulations of optical power distribution within the device were conducted by means of the FDTD method (Lumerical FDTD Solutions). The FDTD model was set as follows: thickness of the FTO layer was 400 nm, thickness of the Cl-TiO$_2$ layer was set to be 30 nm, thickness of the Mp-TiO$_2$ layer was set to be 150 nm for the control group, thickness of the perovskite layer was 550 nm (500 nm pure perovskite layer + 50 nm perovskite which was infiltrated into the Mp-TiO$_2$ layer) and *n*, *k* values of the FA based perovskite were set based on the literature methods[11,57]. The thickness of spiro-OMeTAD layer was 150 nm, and the thickness of Au and ITO was 22.5 and 80 nm, respectively. For the optical power distribution measurement, a monitor was set along the device. The 1D optical model of optical admittance analysis simulations is built based on the same device parameters.

Characterization

J–V characteristics were measured in a glovebox with a solar simulator (SAN-EI Electric XES-301S 300 W Xe Lamp JIS Class AAA) and a Keithley 2400 source meter. Another light source was generated from a flashlight during the *J–V* measurement (the full spectra of the LED light are given in Supplementary Fig. 6). Various neutral density filters (Newport) were used to adjust the light intensity. The solar cells were masked with metal apertures to define the active areas, which were typically 0.09 cm^2. IPCE was recorded with a Keithley 2400 source meter combined with an Oriel 300-W Xe lamp, an Oriel Cornerstone 130 monochromator, and an SRS 810 lock-in amplifier (Stanford Research Systems). A calibrated Si diode was used as the reference. The surface and cross-section morphologies of the samples were investigated by a SEM (JEOL JSM-7001F) at 10 kV. Transmittance spectra were acquired by a UV-VIS-NIR spectrophotometer (UV-3600, SHIMADZU). ICON-PKG atomic force microscopy (AFM) from Bruker was used to investigate the morphological influence of the ITO/Au on the active layer. The X-ray photoelectron spectroscopy (XPS) spectra were collected with a VG ESCALAB 220I-XL system equipped with an Al K α X-ray source (1486.6 eV). The excitation source of UPS was He I (*hv* = 21.2 eV). Photoelectrons were collected by a rotatable hemispherical electron energy analyzer. UPS spectra were measured in normal emission to examine shifts of the secondary electron edge. A 532 nm Nd:YAG pulsed laser

(NT341A–10–AW, pulse duration shorter than 4 ns and 1 Hz repetition frequency) was used as excitation light source in the small perturbation TPV experiments. Neutral density filters were used to afford a small perturbation (below 20 mV) of the cell photovoltage. A white light halogen lamp was employed to provide the back illumination (0.4 V). The TPVs were monitored by a digital oscilloscope (Agilent 54845A). To get the TPV spectra of the dual-side functional device, the light source from the flashlight was added to the ITO side of the device and both the laser beam and the background white light from the halogen lamp shone on the FTO side. The impedance spectroscopy measurement of the solar cells was conducted using an AUTOLAB potentiostat (PGSTAT30) with an AC signal of 20 mV in amplitude, and Z-view v3.1 software was used for equivalent circuit fitting.

DATA AVAILABILITY
Authors can confirm that all relevant data are included in the article and/or its supplementary information files.

REFERENCES
1. Yang, W. S. et al. Iodide management in formamidinium-lead-halide–based perovskite layers for efficient solar cells. *Science* **356**, 1376–1379 (2017).
2. Kojima, A., Teshima, K., Shirai, Y. & Miyasaka, T. Organometal halide perovskites as visible-light sensitizers for photovoltaic cells. *J. Am. Chem. Soc.* **131**, 6050–6051 (2009).
3. Im, J., Lee, C., Lee, J., Park, S. & Park, N. 6.5% efficient perovskite quantum-dot-sensitized solar cell. *Nanoscale* **3**, 4088–4093 (2011).
4. Lee, M., Teuscher, J., Miyasaka, T., Murakami, T. & Snaith, H. Efficient hybrid solar cells based on meso-superstructured organometal halide perovskites. *Science* **338**, 643–647 (2012).
5. Zhou, H. et al. Interface engineering of highly efficient perovskite solar cells. *Science* **345**, 542–546 (2014).
6. Saliba, M. et al. Incorporation of rubidium cations into perovskite solar cells improves photovoltaic performance. *Science* **354**, 206–209 (2016).
7. Ye, T. et al. Electrosprayed TiO2 nanoporous hemispheres for enhanced electron transport and device performance of formamidinium based perovskite solar cells. *Nanoscale* **9**, 412–420 (2017).
8. Jeon, N. J. et al. Compositional engineering of perovskite materials for high-performance solar cells. *Nature* **517**, 476–480 (2015).
9. Saliba, M. et al. Cesium-containing triple cation perovskite solar cells: improved stability, reproducibility and high efficiency. *Energy Environ. Sci.* **9**, 1989–1997 (2016).
10. Bi, D. et al. Polymer-templated nucleation and crystal growth of perovskite films for solar cells with efficiency greater than 21%. *Nat. Energy* **1**, 16142 (2016).
11. Ye, T. et al. Performance enhancement of tri-cation and dual-anion mixed perovskite solar cells by Au@SiO2 nanoparticles. *Adv. Funct. Mater.* **27**, 1606545 (2017).
12. Cacovich, S. et al. Imaging and quantifying non-radiative losses at 23% efficient inverted perovskite solar cells interfaces. *Nat. Commun.* **13**, 2868 (2022).
13. Chen, W. et al. Monolithic perovskite/organic tandem solar cells with 23.6% efficiency enabled by reduced voltage losses and optimized interconnecting layer. *Nat. Energy* **7**, 229–237 (2022).
14. Li, Z. et al. Organometallic-functionalized interfaces for highly efficient inverted perovskite solar cells. *Science* **376**, 416–420 (2022).
15. Bi, D. et al. Efficient luminescent solar cells based on tailored mixed-cation perovskites. *Sci. Adv.* **2**, e1501170 (2016).
16. Chen, Q. et al. Controllable self-induced passivation of hybrid lead iodide perovskites toward high performance solar cells. *Nano Lett.* **14**, 4158–4163 (2014).
17. Stoumpos, C., Malliakas, C. & Kanatzidis, M. Semiconducting tin and lead iodide perovskites with organic cations: phase transitions, high mobilities, and near-infrared photoluminescent properties. *Inorg. Chem.* **52**, 9019–9038 (2013).
18. Hoke, E. T. et al. Reversible photo-induced trap formation in mixed-halide hybrid perovskites for photovoltaics. *Chem. Sci.* **6**, 613–617 (2015).
19. Li, Z. et al. Stabilizing perovskite structures by tuning tolerance factor: formation of formamidinium and cesium lead iodide solid-state alloys. *Chem. Mater.* **28**, 284–292 (2015).
20. Eperon, G. et al. Formamidinium lead trihalide: a broadly tunable perovskite for efficient planar heterojunction solar cells. *Energy Environ. Sci.* **7**, 982–988 (2014).
21. Lee, J., Seol, D., Cho, A. & Park, N. High efficiency perovskite solar cells based on the black polymorph of HC(NH2)2PbI3. *Adv. Mater.* **26**, 4991–4998 (2014).
22. Kulbak, M., Cahen, D. & Hodes, G. How important is the organic part of lead halide perovskite photovoltaic cells? Efficient CsPbBr3 cells. *J. Phys. Chem. Lett.* **6**, 2452–2456 (2015).
23. Møller, C. K. Crystal structure and photoconductivity of caesium plumbohalides. *Nature* **182**, 1436–1436 (1958).
24. Bekenstein, Y., Koscher, B. A., Eaton, S. W., Yang, P. & Alivisatos, A. P. Highly luminescent colloidal nanoplates of perovskite cesium lead halide and their oriented assemblies. *J. Am. Chem. Soc.* **137**, 16008–16011 (2015).
25. Loi, M. A. & Hummelen, J. C. Hybrid solar cells: perovskites under the sun. *Nat. Mater.* **12**, 1087–1089 (2013).
26. Ye, T. et al. Enhanced charge carrier transport and device performance through dual-cesium doping in mixed-cation perovskite solar cells with near unity free carrier ratios. *ACS Appl. Mater. Interfaces* **9**, 2358–2368 (2017).
27. Fujishima, A. & Honda, K. Electrochemical photolysis of water at a semiconductor electrode. *Nature* **238**, 37–38 (1972).
28. Nozik, A. J. p-n photoelectrolysis cells. *Appl. Phys. Lett.* **29**, 150–153 (1976).
29. Murphy, G. W. Model systems in photoelectrochemical energy conversion. *Sol. Energy* **21**, 403–407 (1978).
30. Xiao, K. et al. Scalable processing for realizing 21.7%-efficient all-perovskite tandem solar modules. *Science* **376**, 762–767 (2022).
31. Pham, H. D., Yang, T. C.-J., Jain, S. M., Wilson, G. J. & Sonar, P. Development of dopant-free organic hole transporting materials for perovskite solar cells. *Adv. Energy Mater.* **10**, 1903326 (2020).
32. Pham, H. D. et al. Organic interfacial materials for perovskite-based optoelectronic devices. *Energy Environ. Sci.* **12**, 1177–1209 (2019).
33. Kranthiraja, K. et al. Accomplishment of multifunctional π-conjugated polymers by regulating the degree of side-chain fluorination for efficient dopant-free ambient-stable perovskite solar cells and organic solar cells. *ACS Appl. Mater. Interfaces* **9**, 36053–36060 (2017).
34. Saianand, G. et al. Current advancements on charge selective contact interfacial layers and electrodes in flexible hybrid perovskite photovoltaics. *J. Energy Chem.* **54**, 151–173 (2021).
35. Cai, L. & Zhu, F. Toward efficient and stable operation of perovskite solar cells: Impact of sputtered metal oxide interlayers. *Nano Sel.* **2**, 1417–1436 (2021).
36. Yao, Y. et al. Toward high-performance semitransparent perovskite solar cells: interfacial modification and charge extraction perspectives. *Mater. Today Energy* **21**, 100833 (2021).
37. Cai, L. et al. Mitigation of morphological defects in methylammonium-free formamidinium-based perovskite solar cells. *ACS Appl. Energy Mater.* **5**, 8304–8312 (2022).
38. Kim, M.-G., Kanatzidis, M. G., Facchetti, A. & Marks, T. J. Low-temperature fabrication of high-performance metal oxide thin-film electronics via combustion processing. *Nat. Mater.* **10**, 382–388 (2011).
39. Omer, M. I., Wang, X. & Tang, X. Determination of dominant recombination site in perovskite solar cells through illumination-side-dependent impedance spectroscopy. *Prog. Photovolt. Res. Appl.* **30**, 1228–1237 (2022).
40. You, J. et al. A polymer tandem solar cell with 10.6% power conversion efficiency. *Nat. Commun.* **4**, 1446 (2013).
41. Helander, M. G. et al. Chlorinated indium tin oxide electrodes with high work function for organic device compatibility. *Science* **332**, 944–947 (2011).
42. Odwyer, C. et al. Bottom-up growth of fully transparent contact layers of indium tin oxide nanowires for light-emitting devices. *Nat. Nanotechnol.* **4**, 239–244 (2009).
43. Shen, Y. et al. Modification of indium tin oxide for improved hole injection in organic light emitting diodes. *Adv. Mater.* **13**, 1234–1238 (2001).
44. Freitag, M. et al. Dye-sensitized solar cells for efficient power generation under ambient lighting. *Nat. Photon.* **11**, 372–378 (2017).
45. Burschka, J. et al. Sequential deposition as a route to high-performance perovskite-sensitized solar cells. *Nature* **499**, 316–319 (2013).
46. Hu, T. et al. Indium-free perovskite solar cells enabled by impermeable tin oxide electron extraction layers. *Adv. Mater.* **29**, 1606656 (2017).
47. Zhao, J. et al. Self-encapsulating thermostable and air-resilient semitransparent perovskite solar cells. *Adv. Energy Mater.* **7**, 1602599 (2017).
48. Yee, K. Numerical solution of initial boundary value problems involving Maxwell's equations in isotropic media. *IEEE Trans. Antennas Propag.* **14**, 302–307 (1966).
49. Tavakoli, M. M. et al. Highly efficient flexible perovskite solar cells with antireflection and self-cleaning nanostructures. *ACS Nano* **9**, 10287–10295 (2015).
50. Xing, G. et al. Long-range balanced electron-and hole-transport lengths in organic-inorganic CH3NH3PbI3. *Science* **342**, 344–347 (2013).
51. Dong, Q. et al. Electron-hole diffusion lengths >175 μm in solution-grown CH3NH3PbI3 single crystals. *Science* **347**, 967–970 (2015).

52. Luo, D. et al. Dual source precursor approach for highly efficient inverted planar heterojunction perovskite solar cells. *Adv. Mater.* **29**, 1604758 (2017).

53. Stranks, S. D. et al. Recombination kinetics in organic-inorganic perovskites: excitons, free charge, and subgap states. *Phys. Rev. Appl.* **2**, 034007 (2014).

54. Roiati, V. et al. Investigating charge dynamics in halide perovskite-sensitized mesostructured solar cells. *Energy Environ. Sci.* **7**, 1889–1894 (2014).

55. Bertoluzzi, L. et al. Cooperative kinetics of depolarization in $CH_3NH_3PbI_3$ perovskite solar cells. *Energy Environ. Sci.* **8**, 910–915 (2015).

56. Ndione, P. F., Li, Z. & Zhu, K. Effects of alloying on the optical properties of organic-inorganic lead halide perovskite thin films. *J. Mater. Chem. C* **4**, 7775–7782 (2016).

57. Sacco, A. Electrochemical impedance spectroscopy: fundamentals and application in dye-sensitized solar cells. *Renew. Sustain. Energy Rev.* **79**, 814–829 (2017).

58. Fabregat-Santiago, F., Garcia-Belmonte, G., Mora-Sero, I. & Bisquert, J. Characterization of nanostructured hybrid and organic solar cells by impedance spectroscopy. *Phys. Chem. Chem. Phys.* **13**, 9083–9118 (2011).

59. Pascoe, A. R., Duffy, N. W., Scully, A. D., Huang, F. & Cheng, Y.-B. Insights into planar CH3NH3PbI3 perovskite solar cells using impedance spectroscopy. *J. Phys. Chem. C* **119**, 4444–4453 (2015).

60. Ebadi, F., Taghavinia, N., Mohammadpour, R., Hagfeldt, A. & Tress, W. Origin of apparent light-enhanced and negative capacitance in perovskite solar cells. *Nat. Commun.* **10**, 1574 (2019).

61. Zarazua, I. et al. Surface recombination and collection efficiency in perovskite solar cells from impedance analysis. *J. Phys. Chem. Lett.* **7**, 5105–5113 (2016).

62. Contreras-Bernal, L. et al. Impedance analysis of perovskite solar cells: a case study. *J. Mater. Chem. A* **7**, 12191–12200 (2019).

63. Almora, O. et al. Light intensity modulated impedance spectroscopy (LIMIS) in all-solid-state solar cells at open-circuit. *Nano Energy* **75**, 104982 (2020).

64. Tang, C. W. Two-layer organic photovoltaic cell. *Appl. Phys. Lett.* **48**, 183–185 (1986).

65. Halls, J. J. M., Pichler, K., Friend, R. H., Moratti, S. C. & Holmes, A. B. Exciton diffusion and dissociation in a poly(p-phenylenevinylene)/C60 heterojunction photovoltaic cell. *Appl. Phys. Lett.* **68**, 3120–3122 (1996).

AUTHOR CONTRIBUTIONS

T.Y. and X.W. conceived the experiments; T.Y., X.L., D.W., S.M. and X.W. carried out the device fabrication, characterizations, performance measurements as well as optical simulations. All authors analyzed data and wrote the manuscript.

COMPETING INTERESTS

The authors declare no competing interests.

ADDITIONAL INFORMATION

Supplementary information The online version contains supplementary material available at https://doi.org/10.1038/s41528-023-00256-1.

Correspondence and requests for materials should be addressed to Jianwei Xu, Chellappan Vijila or Xizu Wang.

Reprints and permission information is available at http://www.nature.com/reprints

Publisher's note Springer Nature remains neutral with regard to jurisdictional claims in published maps and institutional affiliations.